Mon. Not. R. Astron. Soc. **000**, 1–10 (2002) Printed 4 August 2016 (MN LATEX style file v2.2)

Observations of the planetary nebula RWT 152 with OSIRIS/GTC⋆

A. Aller[1,2,3]†, L. F. Miranda[4], L. Olguín[5], E. Solano[2,6] and A. Ulla[3,7]
[1]*Instituto de Física y Astronomía, Facultad de Ciencias, Universidad de Valparaíso, Gran Bretaña 1111, Playa Ancha, Valparaíso, 2360102, Chile*
[2]*Departamento de Astrofísica, Centro de Astrobiología (INTA-CSIC), PO Box 78, Villanueva de la Cañada (Madrid) E-28691, Spain*
[3]*Departamento de Física Aplicada, Universidade de Vigo, Campus Lagoas-Marcosende s/n, Vigo E-36310, Spain*
[4]*Instituto de Astrofísica de Andalucía - CSIC, C/ Glorieta de la Astronomía s/n, E-18008 Granada, Spain*
[5]*Departamento de Investigación en Física, Universidad de Sonora, Blvd. Rosales Esq. L.D. Colosio, Edif. 3H, 83190 Hermosillo, Son. Mexico*
[6]*Spanish virtual observatory, PO Box 78, Villanueva de la Cañada (Madrid) E-28691, Spain*
[7]*Astronomy Unit, Queen Mary University of London, Mile End Road, London E1 4NS, UK*

arXiv:1608.01258v1 [astro-ph.SR] 3 Aug 2016

Accepted 1988 December 15. Received 1988 December 14; in original form 1988 October 11

ABSTRACT
RWT 152 is one of the few known planetary nebulae with an sdO central star. We present subarcsecond red tunable filter Hα imaging and intermediate-resolution, long-slit spectroscopy of RWT 152 obtained with OSIRIS/GTC with the goal of analyzing its properties. The Hα image reveals a bipolar nebula with a bright equatorial region and multiple bubbles in the main lobes. A faint circular halo surrounds the main nebula. The nebular spectra reveal a very low-excitation nebula with weak emission lines from H^+, He^+, and double-ionized metals, and absence of emission lines from neutral and single-ionized metals, except for an extremely faint [N II] λ6584 emission line. These spectra may be explained if RWT 152 is a density-bounded planetary nebula. Low nebular chemical abundances of S, O, Ar, N, and Ne are obtained in RWT 152, which, together with the derived high peculiar velocity ($\sim$ 92-131 km s^{-1}), indicate that this object is a halo planetary nebula. The available data are consistent with RWT 152 evolving from a low-mass progenitor ($\sim$ 1 M$_\odot$) formed in a metal-poor environment.

Key words: planetary nebulae: individual: RWT 152 – hot subdwarfs – ISM: abundances.

1 INTRODUCTION

The formation of a planetary nebula (PN) is the last phase in the evolution of low- and intermediate-mass stars (initially 0.8-8 M$_\odot$) before they become white dwarfs. PNe exhibit a wide variety of morphologies and properties that should be closely related to the evolution of their central stars (CSs). PNe host a diversity of CSs. Weidmann & Gamen (2011) compiled 26 spectroscopically well-distinguished types of CSs, that include, for example, hybrid stars, O-type, and hot subdwarf stars (sdOs and sdBs). However, there are only a few PNe known that host an sdO CS. Aller et al. (2015a) (hereafter AM15), list 18 PNe around sdOs CSs. Although this number is probably a lower limit because several CSs still lack a firm classification as, e.g., NGC 1514 (Aller et al. 2015b) and NGC 6026 (De Marco 2009; Hillwig et al. 2010), the number of PN+sdO systems is very small as compared with the large number of known sdOs without associated PNe (see, e.g., Østensen 2006) and with the number of known Galactic PNe ($\sim$ 3000, Frew & Parker 2010). Intriguingly, PNe around sdO CSs share some characteristics: they are generally evolved or relatively evolved PNe ($\sim 10^4$ yr) with a very low surface brightness; most of them present elliptical and bipolar shapes, often with multiple structures, including signs of collimated outflows; and a high fraction of confirmed (or suspected) binary CSs is also observed in these PN+sdO systems (for more details see AM15 and references therein).

The existence of these common characteristics strongly suggests a common formation process for these PNe as well. On the other hand, the small number of these systems points out that some peculiarities may be present in their formation. Among the various evolutionary paths to explain the formation of an sdO star (see Heber 2009), post-asymptotic giant branch (post-AGB) evolution appears as the most suitable one for those sdOs with PNe around them. If so, the small number of these systems implies that PN ejection is a rare evolutionary path for sdOs. However, as sdOs are thought to represent the late stage of low-mass stars (see, e.g., Heber 2009), whose evolution proceeds very slow, the number of PN+sdO systems could be biased due, at least in part, to the fact that the shell ejected during the post-AGB phase could have dispersed before being photoionized. In any case, PN+sdO systems are peculiar and their origin should be investigated. An interesting approximation to study these systems is analyzing the properties

⋆ Based on observations made with the Gran Telescopio Canarias (GTC), installed at the Spanish Observatorio de El Roque de los Muchachos of the Instituto de Astrofísica de Canarias, in the island of La Palma.
† E-mail: alba.aller@ifa.uv.cl (AA)

of the PNe themselves (e.g., morphology, chemical abundances), which may provide clues about their formation and evolution.

RWT 152 ($\alpha_{(2000.0)} = 07^h\,29^m\,58\overset{s}{.}5$, $\delta_{(2000.0)} = -02^\circ\,06'\,37''$; $l = 219\overset{\circ}{.}2$, $b = 7\overset{\circ}{.}5$) is one of the few PNe hosting a CS classified as sdO (Ebbets & Savage 1982). This compact and faint PN was originally discovered by Pritchet (1984) and has recently been analyzed by AM15 by means of narrow-band imaging, and low- and high-resolution long-slit optical spectra. The images by AM15 show a faint bipolar PN in the light of [O III] while a diffuse, non-spherical shape can be distinguished in the light of Hα. The analysis of the internal kinematics by AM15 showed a basic pattern of bipolar motions, although these authors noticed some deviations from a pure bipolar (hour-glass) shell, suggesting a more complex morpho-kinematic structure. In addition, the polar velocity of 19 km s^{-1} derived by AM15 and the published distances of 1.4 and 6.5 kpc (Ebbets & Savage 1982; Pritchet 1984, respectively) to RWT 152, yield a kinematical age of $\simeq$ 6.6 and 17.8 $\times 10^3$ yr, respectively, which suggests an already evolved PN. Finally, only Hα, Hβ, and [O III]$\lambda\lambda$4959,5007 emission lines were detected in the nebular spectra, which leaded AM15 to suggest a possible deficiency of heavy elements in the nebula. Confirmation of this possible deficiency requires much deeper spectra given the faintness of RWT 152. In addition, images at higher spatial resolution are necessary to analyze its morphology in detail. In this framework, large telescopes represent a very useful tool to carry out detailed analyses of such faint PNe, since they provide very high-quality data with relatively short-exposure times.

In this work we present subarcsecond red tunable filter imaging and deep intermediate-resolution, long-slit spectra of RWT 152 obtained with OSIRIS/GTC, with the aim of studying the morphology, physical conditions and chemical abundances of this PN. The images reveal new structures not observed so far while the spectra allow us to detect very faint nebular emission lines not previously detected, allowing us estimates of the chemical abundances in the nebula. The layout of the paper is as follows: in Sect. 2 we summarize the observations and data reduction. Sect. 3 describes the main results derived from the imaging and intermediate-resolution spectra. A discussion of the results is done in Sect. 4 and the main conclusions are summarized in Sect. 5.

2 OBSERVATIONS AND DATA REDUCTION

2.1 Optical imaging

Images of RWT 152 were obtained on 2013 November 6 in service mode (proposal ID GTC4-13B) with OSIRIS (Optical System for Imaging and low-Intermediate-Resolution Integrated Spectroscopy), mounted on the Nasmyth-B focus of the 10.4 m Gran Telescopio Canarias (GTC), at the Observatorio Roque de los Muchachos (La Palma, Canary Islands, Spain). The detector of OSIRIS consists of two Marconi CCD42-82 (2048×4096 pixels) with a 37 pix (binned) gap between them. The maximum unvignetted field of view (FOV) is 7.8×7.8 arcmin. In order to increase the signal-to-noise we chose the standard 2×2 binning mode which provides a plate scale of 0.254 arcsec pixel^{-1}.

The red tunable filter (RTF, Cepa et al. 2003, 2005) was used, which covers the 6510–9345Å wavelength range. When using the RTF, the user must select one of the available Order Sorter (OS) filters in order to isolate the desired order. Thus, we selected the OS filter f657/35 (i.e., that at central wavelength 6572 Å and FWHM of 350 Å) that provides a wavelength range of 6490–6600Å, with the aim of covering the Hα and [N II] $\lambda\lambda$ 6548,6584 Å emission lines from the nebula. The RTF was sintonized with a full width at half-maximum (FWHM) of 20 Å.

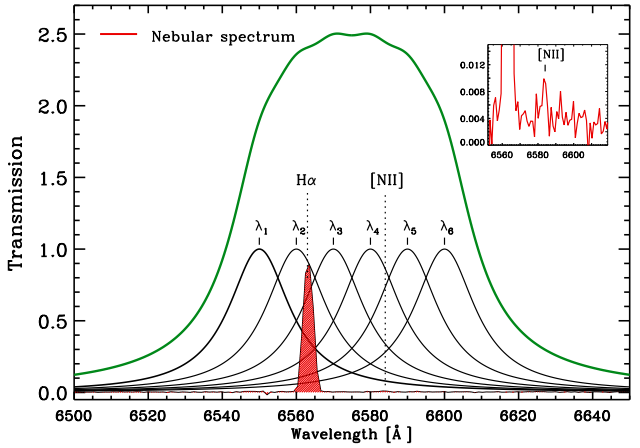

Figure 1. Transmission curves of the OS filter normalized at the peak transmission for the six selected bands (labelled as λ_1, λ_2, λ_3, etc.) are plotted in black. The scaled nebular spectrum of RWT 152 (see Sect. 3.2) is overimposed in red and the position of the Hα and [N II] emission lines is indicated to highlight the contribution of these lines to the different bands. The resulting band of adding each individual band is plotted in green. The inset shows the spectrum in the range 6550–6620 Å, in order to highlighted the weak [N II] λ 6584 Å emission line detected.

It should be noted that with the RTF the wavelength along the FOV is not uniform, decreasing radially outwards from the optical centre following the law

$$\lambda = \lambda_0 - 5.04 \times r(arcmin)^2, \quad (1)$$

where λ_0 is the central wavelength (in angstroms) and r the distance to the optical centre (see González et al. 2014).

This quadratic decrease of the wavelength is particularly critical in extended objects such as PNe, since the light collected from each point of the nebula comes from different wavelengths depending on the distance to the optical centre. Taking this into account, and as mentioned above, the observations were designed to cover the Hα and [N II]λ6548,6584 emissions from all the points of RWT 152. The observing strategy was to obtain images with the optical centre at six different central wavelengths (λ_0 = 6550, 6560, 6570, 6580, 6590, and 6600 Å), hereafter referred to as individual bands. Figure 1 shows the transmission curves of the selected OS filter normalized at the peak transmission centred at these individual bands (black lines) and the positions of the Hα and [N II]λ6584 emission lines are indicated. The intermediate-resolution, long-slit spectrum of RWT 152 (see Sect. 3.2) has also been plotted in Fig. 1 to show the contribution of the Hα and the possible (very faint) [N II]λ6584 emission line detected. We note that the observed flux of the [N II]λ6584 emission line is practically negligible, only ~0.5% of Hα (see Sect. 3.2), thus making the Hα emission line the main contributor in this OS filter. The CS of RWT 152 was placed at ~ 1 arcmin from the optical centre, corresponding to ~ 5 Å bluer than the central wavelength of each band (see equation 1). However, the small size of RWT 152 (see Sect. 3.1) implies that the wavelength along the nebula hardly varies, so we can assume that all points of the nebula are covered by approximately the same wavelength. Therefore, for this particular case, by adding the im-

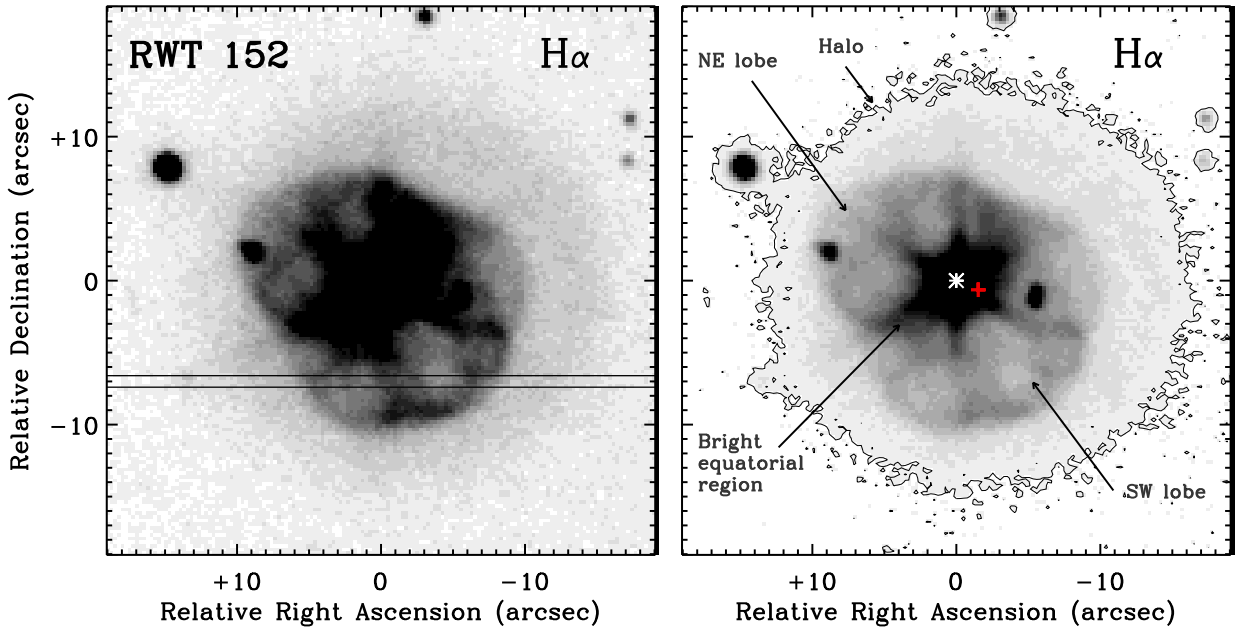

Figure 2. Grey-scale reproductions of the Hα image of RWT 152 (north is up; east to the left). Grey levels are linear on the left-hand panel and logarithmic on the right-hand one. The origin (0,0) is the position of the central star marked with a white asterisk. The long slit used for spectroscopy is indicated by the horizontal lines in the left-hand panel and the different features of the nebula are indicated in the right-hand panel (see text for more details). The contour in the right-hand panel traces the size of the halo at the 3σ level above the background; the geometrical center of the halo is indicated by a red plus symbol.

ages of all individual bands we obtain an Hα image of RWT 152. Three images were taken in each individual band, each with an exposure time of 80 s, allowing a dithering of ~5 arcsec between images to properly remove the diametric ghosts produced in the images.

The images were reduced using the standard procedures within IRAF[1]. After correcting each individual frame from bias and flat-field, the three images of each individual band were aligned and median combined. Then, we added all images of all individual bands to obtain a deep Hα image within the total band plotted as a green line in Fig 1. The total exposure time for the final Hα image is 1440 s (i.e., 6(bands)×3(images)×80 s) and the spatial resolution is 0.7 arcsec, as indicated by the FWHM of field stars in the image. Figure 2 shows the Hα image at two different grey levels. We note that the Hα image contains some contribution of the nebular continuum (see Fig. 1). Nevertheless, as we will see below, this contribution is very small and the final Hα image in Fig 1 can be considered as representative of the "pure" Hα emission.

2.2 Intermediate-resolution, long-slit optical spectra

Intermediate-resolution, long-slit spectra of RWT 152 were obtained with OSIRIS. The volume-phased holographic gratings (VPHs) R2500U, R2500V, R2500R, R2500I were used. They cover the spectral ranges 3440–4610, 4500–6000, 5575–7685, and 7330-10000 Å, respectively, at dispersions of 0.62, 0.80, 1.04, and 1.36 Å pixel^{-1} (these dispersions are measured at central wavelengths for a slit width of 0.6 arcsec). The standard 2×2 binning mode was used, which provides a plate scale of 0.254 arcsec pixel^{-1}.

Spectra were obtained on 2013 November 6 (R2500R, R2500I) and 7 (R2500U, R2500V). The slit width was 0.8 arcsec and the spectra were obtained with the slit oriented at PA 90° and centred 7 arcsec south of the CS (see Fig. 2, left panel), covering the southwestern lobe of the nebula. The exposure time was 1200 s for each VPH and the seeing was ≃ 0.9 arcsec.

The spectra were reduced following standard procedures for long-slit spectroscopy within the IRAF and MIDAS[2] packages. The reduction included cosmic rays removal, bias subtraction and flat-field correction. Then, the spectra were wavelength calibrated, sky subtracted and, finally, flux calibrated using the spectrophotometric standard Hiltner 600. Some differences (less than 1%) were found in the calibrated fluxes of the standard star in the overlapping range of the VPHs, which translate to the flux calibration of the nebular spectra. Nevertheless, these differences are within the uncertainties of the flux calibration process. Finally, we note that strong sky lines in the nebular spectrum could not be completely removed, leaving some residuals that prevent us from a clear identification or measurement of some nebular emission lines. This problem is particu-

[1] IRAF is distributed by the National Optical Astronomy Observatory, which is operated by the Association of Universities for Research in Astronomy (AURA) under a cooperative agreement with the National Science Foundation.

[2] MIDAS is developed and maintained by the European Southern Observatory.

larly accused in the spectrum obtained with the VPH R2500I where most sky lines could not be removed (see Sect. 3.2).

3 RESULTS

3.1 Morphology

The high quality and subarcsecond resolution of the OSIRIS/GTC Hα image (Fig. 2) allow us to describe new morphological structures in RWT 152 not detected so far, improving substantially the previous description by AM15. The nebula shows a clear bipolar morphology in the light of Hα with a size of $\simeq$ 17×21 arcsec^2 and the major axis oriented at PA $\sim$ 45°, that are compatible with the size and orientation measured by AM15 in their [O III] image. However, the new image reveals that the bipolar lobes are slightly different from each other, being the SW lobe broader than the NE one and that they are composed by many bubbles, specially well defined in the SW lobe. No point-symmetric distribution of the bubbles is noticed in the Hα image. The presence of these small bubbles may explain the deviations from a pure hour-glass geometry observed in the high-resolution, long-slit spectrum along the major nebular axis (AM15).

The Hα image also shows that the equatorial region of the bipolar shell is particularly bright (Fig. 2, more evident in the left panel). To check the veracity of this structure and to discard possible effects produced by the brightness of the CS, we inspected the RTF image in the individual band with the optical centre at λ_6=6600 Å (see Fig. 3), where the emission should be dominated by the nebular continuum, although with a small contribution of Hα and even much smaller of [N II]. In this image, the bright equatorial region cannot be recognized, indicating that this region corresponds to a real nebular structure that is most probably associated to the equatorial torus identified in the high-resolution, long-slit spectra (AM15). In Fig. 2, the CS appears displaced $\sim$ 3 arcsec northwards with respect to the centre of the nebula. This value slightly differs from the displacement inferred from the high-resolution spectra, where a shift of $\simeq$ 1.4 arcsec towards PA $\simeq$ 348° was obtained (AM15). However, as the new image does not allow us to trace clearly the torus, the displacement obtained from the high-resolution spectra should be considered as a more precise value.

Finally, a very faint circular halo of $\sim$ 29 arcsec in diameter can be recognized in the Hα image (see Fig. 2, right panel). Neither the main nebula nor the CS are centred in the halo but are clearly displaced towards the northeast with respect to the geometrical center of the halo. Displacements of a halo with respect to the CS and PN have been traditionally attributed to interaction of the PN with the ISM (see, e.g., Ramos-Larios & Phillips 2009). In the case of RWT 152, the displacements suggest that the east/southeast region of the halo is interacting with the ISM. Nevertheless, if so, one would expect that the east/southeast part of the halo would be the brightest one, which is not observed in our image. In addition, the halo does not show departures from a circular symmetry, as it could be expected from that interaction. Higher-resolution images would be helpful to confirm this possible interaction.

3.2 The optical spectrum: physical conditions and chemical abundances

Figure 4 shows the intermediate-resolution, long-slit spectra of RWT 152, both inner nebula (upper panel) and halo (lower panel), obtained by combining the VPHs R2500U, R2500V and R2500R.

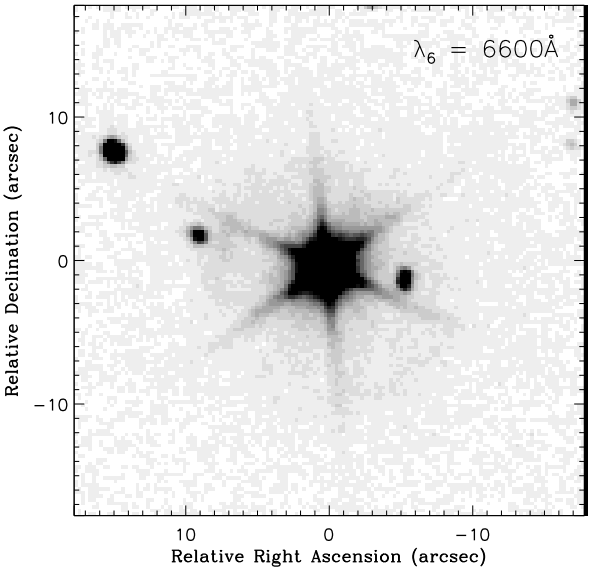

Figure 3. Grey-scale reproduction of the RTF image with the optical centre at λ_6=6600 Å, where the contribution of the Hα emission line is minimum (see figure 1). Grey levels are linear.

The VPH R2500I is not shown here because of the strong contamination by the sky lines (Sect. 2.2, but see also below). For the case of the inner nebula, the spectra have been obtained by integrating the detected emission lines between 4 and 6.4 arcsec west of RWT 152 along the slit. This region corresponds to that showing the highest signal-to-noise ratio for the weakest lines (e.g., [O III]λ4363). Whereas only Hα, Hβ and [O III]$\lambda\lambda$4959,5007 emission lines had been previously detected in RWT 152 (AM15), the long-exposure OSIRIS/GTC spectra reveal other faint nebular emissions. In particular, [Ar III], [Ne III] and He I emission lines are detected. The [N II]λ6584 emission line could also be present, although its extreme faintness (observed flux $\sim$ 1.32 $\times10^{-17}$ erg cm^{-2} s^{-1}) suggests to take this identification with caution. In the VPH R2500I the [S III]$\lambda\lambda$9069,9532 emission lines are clearly identified and relatively isolated from strong sky lines whereas other faint emission lines ([Ar III]λ7751, some Paschen lines) could also be present. Emission lines due to [N I], [O I], [O II] and [S II] are not identified. This result is entirely compatible with the lack of these emission lines in the CAFOS spectra and allow us to conclude that emission lines from neutral and single-ionized metals are not present in the spectrum of RWT 152 (except for the possible [N II]λ6584 emission line). Finally, He II emission lines are neither identified.

The spectra of the halo (Fig. 4, lower panel) have been integrated in two 6.35 arcsec regions eastwards and westwards of RWT 152 along the slit. These regions have been added to obtain a higher S/N. Besides the Balmer and [O III]$\lambda\lambda$4959,5007 emission lines, the spectrum of the halo also shows the He Iλ5876 emission line.

The spectra of the inner nebula have been analyzed using the nebular analysis software ANNEB (Olguín et al. 2011), which also integrates the NEBULAR package of IRAF/STSDAS (Shaw & Dufour 1995), for deriving physical conditions and both ionic and elemental abundances. A set of extinction laws are also included and a proper error propagation is performed. Briefly, ANNEB obtains the logarithmic extinction coefficient c(Hβ) and the electron

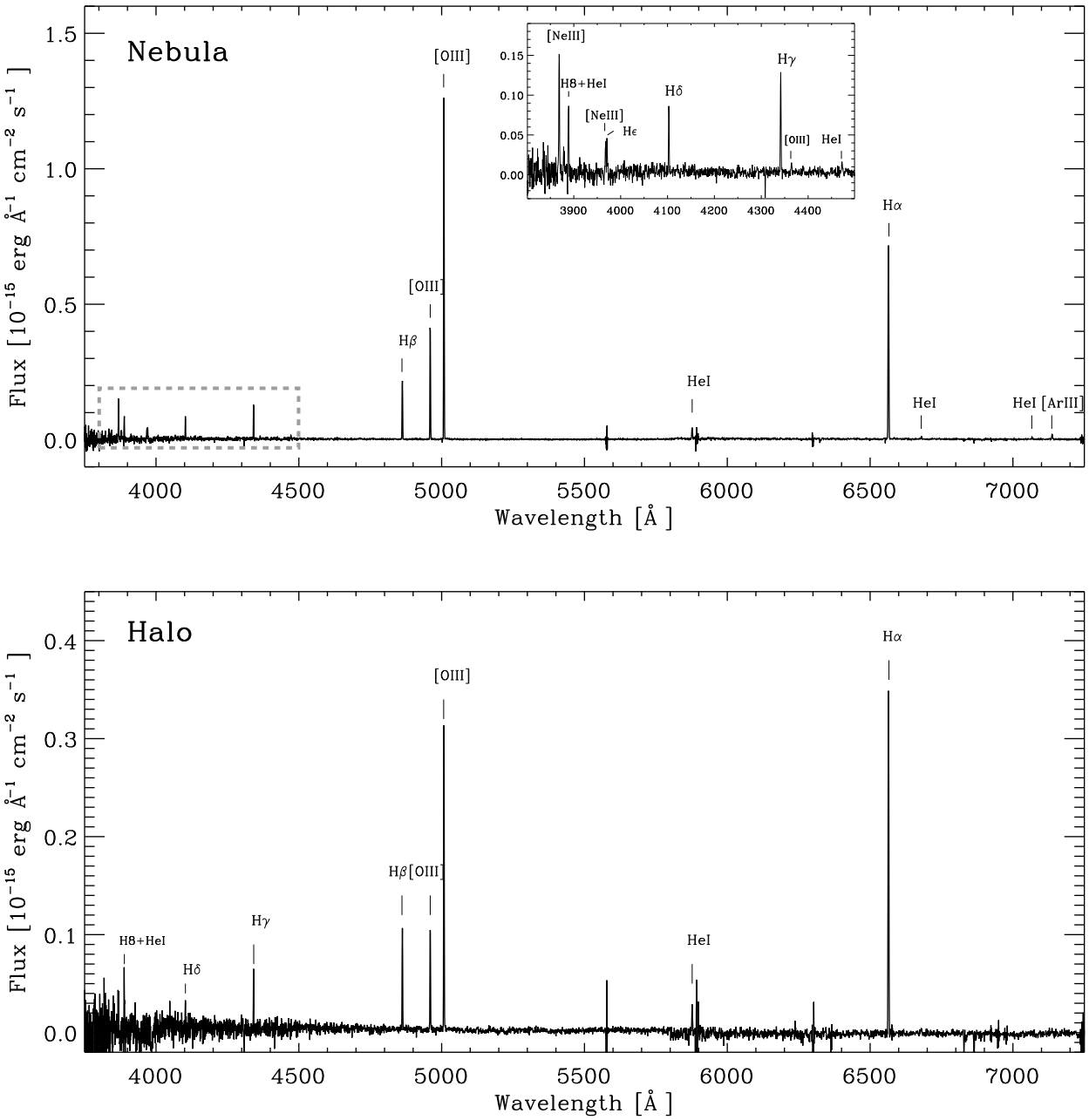

Figure 4. Optical spectrum of the main nebula of RWT 152 (upper panel) and the halo (lower panel) in the spectral range 3800–7250 Å. The VPHs R2500U, R2500V and R2500R have been combined. The detected emissions lines are labelled. The inset in the upper panel shows the spectrum of the inner nebula in the range 3800–4500 Å. For the case of the inner nebula, the spectra have been obtained by integrating the detected emission lines between 4 and 6.4 arcsec west of RWT 152 along the slit (see text). The spectra of the halo (lower panel) have been integrated in two 6.35 arcsec regions eastwards and westwards of RWT 152 along the slit.

temperature from the intensity ratio I(4959+5007)/I(4363) (i.e., T_e ([O III])), iteratively, starting with the values derived for $T_e = 10^4$ K and the theoretical Hα/Hβ line intensity ratio for case B recombination in the low-density limit (Osterbrock & Ferland 2006); then, it derives the dereddened line intensities that are used to calculate the values of c(Hβ) and T_e ([O III]) again. The process is repeated until c(Hβ) and T_e ([O III]) converged to the final values.

A value for the electron density (N_e) is also necessary for the calculations. Unfortunately, the lack of the [S II], [Ar IV] or [Cl III] emission lines from RWT 152 prevents us from deriving N_e from the forbidden lines. Therefore, we have used the observed flux in Hα (F(Hα)) to calibrate the image and the formulation by Hua & Kwok (1999) to calculate the mean electron density in

Table 1. Dereddened emission line intensities in RWT 152.

Line	$f(\lambda)$	Nebula (2.4 arcsec[1])		Halo (12.70 arcsec[1])	
		F_λ(observed)	I_λ(corrected)	F_λ(observed)	I_λ(corrected)
[Ne III] λ3869	0.228	52.0 ± 2.9	70.4 ± 4.3	–	–
He I + H8 λ3889	0.223	31.7 ± 1.8	42.7 ± 2.6	46.9 ± 6.4	63.8 ± 8.7
[Ne III] λ3968	0.203	9.0 ± 0.9	11.9 ± 1.2	–	–
Hϵ λ3970	0.203	14.3 ± 1.0	18.9 ± 1.4	–	–
Hδ λ4101	0.172	24.9 ± 1.1	31.4 ± 1.4	30.5 ± 3.7	38.7 ± 4.8
Hγ λ4340	0.129	40.5 ± 1.5	48.3 ± 1.9	44.1 ± 2.2	52.8 ± 2.7
[O III] λ4363	0.124	7.6 ± 0.5	9.0 ± 0.6	–	–
He I λ4471	0.115	5.8 ± 0.3	6.6 ± 0.4	–	–
Hβ λ4861	0.000	100.0 ± 2.9	100.0 ± 2.9	100.0 ± 2.8	100.0 ± 2.8
[O III] λ4959	−0.023	194.4 ± 4.9	188.2 ± 4.7	104.4 ± 2.7	101.0 ± 2.6
[O III] λ5007	−0.034	579.6 ± 15.0	552.7 ± 14.4	300.6 ± 6.8	286.2 ± 6.5
He I λ5876	−0.216	27.0 ± 0.8	20.2 ± 0.7	28.3 ± 1.5	20.9 ± 1.2
Hα λ6563	−0.323	438.0 ± 11.3	282.5 ± 11.0	451.6 ± 10.5	287.0 ± 10.5
[N II] λ6584(?)	−0.326	2.4 ± 0.1	1.2 ± 0.3	–	–
He I λ6678	−0.338	5.1 ± 0.3	3.2 ± 0.3	–	–
He I λ7065	−0.383	4.8 ± 0.2	2.8 ± 0.3	–	–
[Ar III] λ7135	−0.391	11.0 ± 0.3	6.5 ± 0.3	–	–
[S III] λ9069	−0.606	6.9 ± 0.2	3.0 ± 0.2	–	–
[S III] λ9532	−0.620	21.8 ± 0.6	9.2 ± 0.6	–	–
$\log F_{H\beta}$(erg cm^{-2} s^{-1})			−15.84		-16.20

[1] Size of the region where the long-slit spectra were integrated (see text).

RWT 152. We considered a total flux corrected for extinction[3] of $F_0(H\alpha) = 5.03 \times 10^{-13}$ erg cm^{-2} s^{-1}, observed in a region of 0.8 × 29 arcsec^2 (defined by the slit width and the angular size of the nebula, including the halo), and obtained $N_e = 91\times D[kpc]^{-1/2}$. For distances of 2.4 kpc (Ebbets & Savage 1982) and 6.5 kpc (Pritchet 1984), the electron density is 59 and 36 cm^{-3}, respectively, with an estimated error of about 10% in both cases. No particular differences were noticed in the resulting parameters and ionic and elemental abundances by using one or other of the derived electron density values. We have adopted $N_e = 50 \pm 10$ cm^{-3}.

After the iteration procedure in ANNEB, we obtain $c(H\beta) = 0.59 \pm 0.04$ (calculated from the Hβ and Hα fluxes) and $T_e([O\,III]) = 14000 \pm 550$ K, that are listed in Table 1. ANNEB also provides the $c(H\beta)$ value calculated from other hydrogen lines, as Hγ, for which a consistent value of 0.49± 0.10 is obtained. Also, the $c(H\beta)$ obtained for the halo (0.61± 0.04) is compatible with these results. We note that all these values of $c(H\beta)$ derived from the OSIRIS spectra are slightly higher than (but still compatible with) that obtained by AM15 ($c(H\beta) \sim 0.46$), suggesting internal variations of the extinction in the nebula. On the other hand, according to Schlegel, Finkbeiner & Davis (1998), E(B-V) towards RWT 152 is ∼ 0.1, implying $c(H\beta) \sim 0.15$ (if Rv = 3.1 is assumed), that is very different from the value of ∼ 0.6 derived by us. This large difference would imply a large amount of internal reddening in the nebula, which would not be expected for such a low-density nebula evolved from a low-mass progenitor (see Section 4.1). Alternatively, the difference could be due to the existence of small scale structure in the Galactic dust distribution towards RWT 152, at scales well below ∼ 6 arcmin that is the spatial resolution of the maps by Schlegel, Finkbeiner & Davis (1998). If such a small scale structure exists, it would be undetectable in the maps by Schlegel et al. but could be revealed by observations at much higher spatial resolution than 6 arcmin, as is the case of our spectra where we can measured the extinction at spatial scales of a few arcseconds. In any case, the extinction towards RWT 152 deserves further investigation.

[3] For the calculations of N_e we have used $c(H\beta) = 0.58$, calculated from the observed Hβ and Hα fluxes, that is virtually identical to the value of 0.59 obtained after the iteration procedure with ANNEB, see below.

Table 2. Mean ionic abundances relative to H^+ of RWT 152.

Ion	Ionic abundance
He^+	0.139±0.004
O^{++}	(7.0±0.1)×10^{-5}
N^+	(1.3±0.1)×10^{-7}
Ar^{++}	(2.9±0.1)×10^{-7}
Ne^{++}	(1.8±0.1)×10^{-5}
S^{++}	(2.9±0.1)×10^{-7}

Table 1 lists the observed emission line fluxes and dereddened emission line intensities and their Poissonian errors, both for nebula and halo spectra, where the emission line fluxes have been dereddened with $c(H\beta) = 0.59$ and the extinction law $f(\lambda)$ of Seaton (1979). We further note that the use of other extinction laws (e.g., Cardelli, Clayton & Mathis 1989) does not produce appreciable differences in the dereddened emission line intensities and other parameters.

The absence of the He II λ4686 emission line and the [O III]/Hβ line intensity ratio of ≃ 8 (Table 1) indicate a very low-excitation PN, with an excitation class of 2 according to Gurzadian & Egikian (1991). We note that RWT 152 was erroneously classified as a relatively high-excitation PN by AM15. The very low-excitation is compatible with the relatively low effective temperature of the CS of RWT 152 (≃ 45000 K, Ebbets & Savage 1982). In these circumstances, the non-detection of neutral and single-ionized emission lines (e.g., [S II], [O I], [N I], [O II]) and the extremely faintness of the (possible) [N II]λ6584 emission line is highly peculiar for this excitation class. Under these conditions, one could expect

Table 3. Elemental abundances of RWT 152[1] and average abundances for type III and type IV PNe taken from Costa et al. (1996).

Element	Abundance	Type III PNe	Type IV PNe
He/H	0.139±0.004	0.099	0.104
ϵ(O/H)	7.85±0.02	8.42	8.08
ϵ(N/H)	5.11±0.03	7.74	7.41
ϵ(Ar/H)	5.73±0.02	6.07	5.22
ϵ(Ne/H)	7.26±0.03	7.71	7.27
ϵ(S/H)	5.52±0.08	6.74	5.64

[1] See text for how the elemental abundances have been obtained.

that emission lines due to, e.g., O^0, O^+, S^+, N^0, were prominent even though the abundances of O, S, N were low. This spectrum can be understood if RWT 152 is a density-bounded PN with no low-excitation region (at least along the bipolar lobes, because the equatorial structure has not been studied). In fact, [O I], [N II], [S II] emission lines become very weak in density-bounded models (see Gesicki & Zijlstra 2003), and, in addition, a PN becomes optically thin if the effective temperature of the CS is in the range 40000–50000 K (Kaler & Jacoby 1991), as it is the case of RWT 152.

The derived ionic abundances (i.e., the number density ratio relative to the H^+ number density), calculated as a weighted average by the signal-to-noise ratio of each line for species with more than one line, are listed in Table 2. To obtain the helium abundance, we used the method by Kwitter & Henry (2001), while for the argon abundance, we followed the method by Kingsburgh & Barlow (1994) and used an icf = 1.87, since no [Ar II] is observed. These helium and argon elemental abundances are listed in Table 3, where ϵ(X/H) = log(X/H) + 12 is given (being 12 the hydrogen number density).

For the rest of the elements, the absence of some emission lines prevents to calculate the icfs and, therefore, the elemental abundances. Nevertheless, the low effective temperature of the CS and the observed spectrum allow us to make some reasonable assumptions to obtain approximate values for the abundances. In particular, the lack of He II and [Ar IV] emission lines in the spectra makes it highly improbable that ionization states as O^{3+} and Ne^{3+} may exist in the nebula. This, and the absence of emission lines from O^0, O^+, and Ne^+ in the spectrum of RWT 152 strongly suggest that O^{2+} and Ne^{2+} are the dominant excitation states. In consequence, their ionic abundances may be considered as representative of their elemental abundances and those are listed in Table 3.

In the case of sulfur, if we assume that the ionic abundance of S^{2+} is representative of the elemental sulfur abundance, the elemental abundance would be 5.46. However, this assumption is probably erroneous for sulfur because even if He II and [Ar IV] emission lines are unseen, faint [S IV] emission lines, as, e.g., at 10.52 μm, may be detected in infrared spectra of some low-excitation PNe with relatively cool CSs. In fact, the existence of O^{2+} (ionization potential = 35.1 eV) suggests that S^{3+} (ionization potential = 34.8 eV) may also exists in RWT 152. This is the case of K 648, a very similar object to RWT 152, with an sdO central star of $T_{\rm eff}$ = 37000 K Otsuka, Hyung & Tajitsu (2015); Heber, Dreizler & Werner (1993); Bianchi et al. (2001). As far as we know, there is no available infrared spectrum of RWT 152. Therefore, for comparison purposes, we have estimated the contribution of [S IV] to the total abundance of sulfur in the case of K 648 with the data provided by Otsuka, Hyung & Tajitsu (2015). Our calculations show that the elemental abundance of sulfur reported by Otsuka, Hyung & Tajitsu (2015) is reduced by ~ 15% if the contribution of the [S IV]λ10.52 μm emission line is not considered. If we assume a similar contribution of a (possible) [S IV]λ10.52 μm emission line to the total abundance of sulfur in RWT 152, the value of 5.46 would increase to 5.52. From these calculations and taking into account the differences between K 648 and RWT 152, we will consider in Table 3 a value for the elemental sulfur abundance in RWT 152 of 5.52 ± 0.08, where the error is probably an upper limit to the actual error.

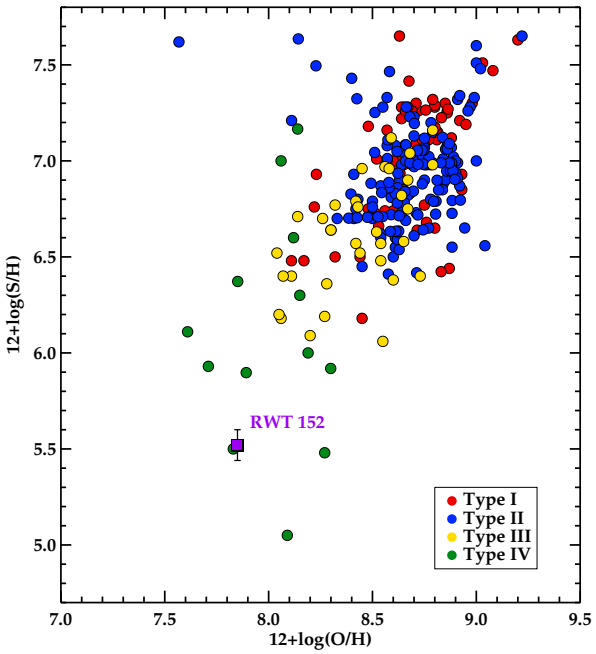

Figure 5. Plot of 12+log(Ar/H) versus 12+log(O/H) (left panel) and 12+log(S/H) versus 12+log(O/H) (right panel) for a sample of type I (red), type II (blue), type III (yellow) and type IV (green) PNe. Data from Henry, Kwitter & Balick (2004), Costa et al. (1996), Maciel & Koppen (1994), Howard, Henry & McCartney (1997), and Pereira & Miranda (2007). The position of RWT 152 is marked with a purple square.

Finally, the nitrogen abundance in RWT 152 is the most uncertain one. We note that N^{2+} may exist in the nebula since other especies with higher ionization potential, like O^{2+}, are also detected. We have inspected the International Ultraviolet Explorer (IUE) spectra of RWT 152 to search for the presence of the semi-forbidden N III] $\lambda\lambda$1747,1754 emission lines. However, there is no traces of these emission lines although they should be prominent if the abundance of N is within the range of values observed in PNe. Therefore, it seems that N^{2+} does not exist in the nebula. Taking this into account and that emission lines due to N^0 neither exist, the N abundance should be similar to the abundance of N^+ and this is quote in Table 3. Nevertheless, given the extreme faintness of the [N II]λ6584 (see above), the existence of nitrogen in the nebula is questionable and, in any case, the elemental abundance in Table 3 should be considered as an upper limit. This result is very surprising for a PN. Nitrogen may not have been produced during the evolution of RWT 152 by the second dredged up. However, this mechanism alone hardly explains the extremely low N abundance or, even, its absence in RWT 152. As additional possibilities we may consider that RWT 152 has been formed in a very nitrogen-

poor environment and/or that nitrogen is depleted (forming part of grains). In any case, a reasonable explanation has not been found.

Table 3 shows low elemental abundances of metals, confirming the previous suggestion by AM15. We will discuss below the implications of these elemental abundances. It is worth noting that the low metal abundances found in RWT 152 provides strong support for a deficiency in metals in 2M 1931+4324, another PN+sdO system with a nebular spectrum very similar to that of RWT 152 (Aller et al. 2013, see also above).

4 DISCUSSION

4.1 Chemistry and evolutionary status of RWT 152

To obtain information about the progenitor of the CS of RWT 152, it is interesting to classify RWT 152 according to the Peimbert (1978) types. Peimbert (1978) classified PNe into four types on the basis of their chemical composition, spatial distribution and kinematical properties. Type I PNe are those with high He and N (He/H $\geqslant$ 0.125; log(N/O) $\geqslant$ -0.30, see Peimbert & Torres-Peimbert (1983)) and they are the youngest population. Type II PNe are the intermediate population, generally older than type I PNe and, therefore, more deficient in heavy elements and without He and N enrichments. Type III PNe belong to the thick disk and present peculiar velocities of $|\ \Delta V_{pr}\ | \geqslant 60$ km s^{-1}, which is the difference between the observed radial velocity and that expected on the basis of Galactic rotation (assumed circular). Finally, type IV PNe are halo objects with $|\ \Delta V_{pr}\ | \geqslant 60$ km s^{-1} and log (O/H)+12 $\leqslant$ 8.1; they correspond to the oldest population.

The helium abundance derived for RWT 152 (He/H $\sim$ 0.140, Table 3) indicates a type I or type II PN. However, the extremely low (or absent) nitrogen abundance rules out these two types. A comparison of the abundances of O, S, Ar and Ne with those typical of type III and type IV PNe, shown in Table 3, indicates that RWT 152 is a type IV PN. To reinforce this classification, we show in Figure 5 the 12+log(S/H) versus 12+log(O/H) diagram for the four Peimbert types of PNe, in which RWT 152 is placed in the region of halo PNe. Finally, it is worth mentioning that the helium abundance in RWT 152 appears high for type IV PNe, although some halo PNe do present relatively high helium abundances, as, e.g., M 2-7 with He/H $\sim$ 0.137 (Quireza, Rocha-Pinto & Maciel 2007).

Moreover, we have derived the peculiar velocity of RWT 152 from its heliocentric radial velocity $V_{\rm HEL}$ $\sim$ +134.5$\pm$1.8 km s^{-1} (AM15), following the formulation explained in Peña, Rechy-García & García-Rojas (2013), and the resulting value is $\sim$ 92 - 131 km s^{-1} for distances of 2.4 kpc and 6.5 kpc, respectively, in any case $\geqslant$ 60 km s^{-1} (see above), confirming the type IV classification for RWT 152. Finally, we note that the height above the Galactic plane of RWT 152 is 0.2–0.8 kpc for the mentioned distances. Although type IV PNe are usually located at z > 0.8 (Peimbert 1990), other halo PNe are located at comparable heights above that plane (see Pereira & Miranda 2007, and references therein). Summarizing, the chemical abundances and the peculiar velocity add RWT 152 as a new member of the few known halo PNe.

A comparison of the He and O abundances in RWT 152 with evolutionary models of stellar yields by Marigo (2001) suggests a progenitor star with an initial mass of $\sim$ 1.3 M$_\odot$ and very low metallicity Z = 0.004. The stellar mass is compatible with that expected for sdOs (Heber 2009) and the low metallicity indicates

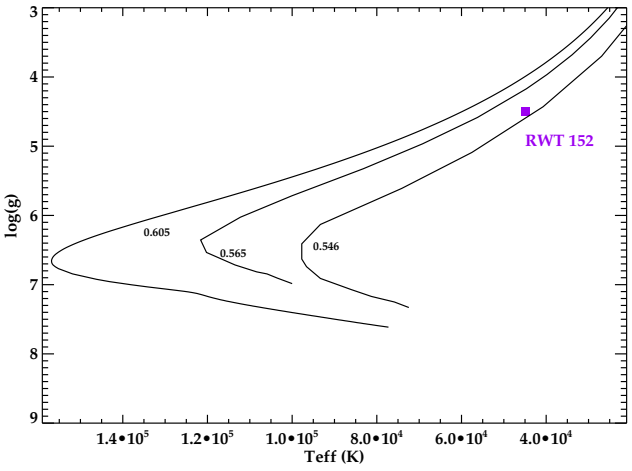

Figure 6. Position of RWT 152 in the $\log g - T_{\rm eff}$ diagram according to Ebbets & Savage (1982). Post-AGB by evolutionary tracks by Bloecker (1995) and Schoenberner (1983) are drawn and labelled with the corresponding stellar mass (in M$_\odot$).

that the progenitor was formed in a poor-metal environment. In contrast, similar models of initial mass $\sim$ 1.25 M$_\odot$ and Z = 0.004 by Karakas (2010) predict abundances substantially different from those found in RWT 152. Even for the lowest metallicity in the Karakas models (Z = 0.0001), we do not recover the chemical abundances of RWT 152. Therefore, it is clear that drawing conclusions about the progenitor star of RWT 152 from the chemical abundances of the nebula may be a bit misleading. For this reason, we have obtained information about the progenitor from the current status of its CS. Figure 6 shows the position of RWT 152 in the HR diagram $\log g - T_{\rm eff}$ with the post-AGB tracks by Bloecker (1995) and Schoenberner (1983). The location of the star ($T_{\rm eff} \simeq$ 45 000 K, $\log g \simeq$ 4.5; Ebbets & Savage 1982) is consistent with a current mass of M$\sim$0.55 M$_\odot$ which implies an initial mass in the main sequence of $\sim$ 1 M$_\odot$. For such a low-mass star, the ejected mass during the AGB evolution is expected to be small. In fact, with the electron density derived above and the size of the nebula we obtain values of 1.3$\times$10^{-2} - 1.6$\times$10^{-1} M$_\odot$ for the ionized nebular mass (assuming 2.4 and 6.5 kpc, respectively, and a filling factor of 0.6). These values are much smaller than ionized masses usually obtained for PNe (see, e.g., Hua & Kwok 1999), further supporting a low-mass progenitor for RWT 152. Moreover, taking into account that 0.1-0.3 M$_\odot$ are lost in the RGB phase of a low-mass star (Dorman, Rood & O'Connell 1993), the current mass of the CS and the obtained ionized mass, we recover a progenitor star with a $\sim$ 0.8-1.0 M$_\odot$, in agreement with the value obtained from the position of the CS in the $\log g - T_{\rm eff}$ diagram. Such a low ionized mass, combined with a relatively high kinematical age, may explain the low surface brightness of RWT 152. If a low-mass progenitor is involved in the evolution of other PNe+sdO systems, it is not surprising that these PNe are very faint and, in some cases, may have faded beyond detection.

4.2 The morphology of RWT 152

The GTC image shows that RWT 152 presents multiple bubbles in its bipolar lobes. The number of PNe with multiple bubbles (or lobes) has largely increased, mainly due to increasing reso-

lution of imaging capabilities. PNe with multiple bubbles/lobes can be classified in two broad categories: (1) those with a point-symmetric distribution of the bubbles/lobes as, e.g., NGC 6058 (Guillén et al. 2013), starfish-like PNe (Sahai 2000), and other young PNe (Sahai & Trauger 1998); and (2) those with a random (non-point-symmetric) distribution of the bubbles/lobes as, e.g., NGC 1514 (Ressler et al. 2010), NGC 7094 and Abell 43 (Rauch 1999). RWT 152 seems to be an intermediate case: it shares with NGC 1514 and Abell 43 the random distribution of the bubbles but also shares with starfish PNe the existence of a bright equatorial region (torus) separating two main lobes (or multiple point-symmetric lobes).

Several scenarios have been proposed to explain the presence of multiple bubbles/lobes, including bipolar jets at several directions with variable ejection velocity (e.g., Velázquez et al. 2012), interaction of a fast wind with a warped circumstellar disk (Rijkhorst, Mellema & Icke 2005), and interaction of a fast wind with a inhomogenous spherical shell (Steffen et al. 2013). Multiple point-symmetric bubbles/lobes appear more compatible with a bipolar jet model or warped disk model than with an inhomogenous shell scenario; the latter would require an extremely point-symmetric density distribution in the spherical AGB shell, which could be difficult to explain. PNe with randomly distributed bubbles could be better explain by an inhomogenous shell. In the case of RWT 152, the random distribution of the bubbles points out to a model in which a dense equatorial torus exists in the spherical shell while the rest of the shell presents an inhomogenous density distribution. Alternatively, wind interaction with a warped disk could also explain random bubbles if material in the two sides of the disk is distributed in a inhomogenous manner. Nevertheless, a definitive conclusion about the shaping of RWT 152 is difficult to be reached because it is an already evolved PNe and the original shaping mechanism could be masked by other processes (e.g., hydrodynamical instabilities). Images of RWT 152 at higher spatial resolution and, in particular, of its equatorial region would be very useful to complete description of the nebula.

5 CONCLUSIONS

We have presented OSIRIS/GTC red tunable filter Hα imaging and intermediate-resolution, long-slit spectroscopy of RWT 152, one of the few known PNe hosting an sdO central star. The data, obtained at subarcsec spatial resolution, allowed us to describe the detailed morphology and to obtain the physical conditions and chemical abundances of the nebula. The main conclusions of this work can be summarized as follows:

(1) The new Hα image shows that RWT 152 is a bipolar PN with a bright equatorial torus, surrounded by a circular halo. The bipolar lobes consist of multiple bubbles with a non point-symmetric distribution. The center of the halo does not coincide with the center of nebula and with the central star, suggesting interaction of the halo with the interstellar medium.

(2) The nebular spectra reveal very faint [Ar III], [Ne III], He I, [S III] emission lines, which had not been previously detected. Emission lines due to neutral and single-ionized metals are not detected, except for an extremely faint [N II]λ6584 emission line, while the lack of He II emission lines indicates that high ionization states (e.g., O^{3+}, S^{3+}, N^{3+}) are probably not present in the nebula. These results strongly suggests that RWT 152 is a density-bounded PN, at least in the direction of the bipolar lobes.

(3) An electron temperature T_e([O III]) of $\sim$ 14000 K and a very low electron density $N_e \sim 50$ cm^{-3} have been obtained for the nebula.

(4) Except for helium, the derived chemical abundances of S, O, Ne and Ar are low. The abundance of N seems to be extremely low and an explanation for this fact has not been found yet. The low abundances and the high peculiar velocity of the object ($|\ \Delta V_{pr}\ | \sim$ 92-131 km s^{-1}) strongly suggest that RWT 152 is a halo PN, adding a new member to the small number of known PNe in this type.

(5) A comparison of the atmospheric parameters of the CS with post-AGB evolutionary tracks suggests a $\sim$ 1.0 $M_\odot$ progenitor for RWT 152, that should be formed in a metal-poor environment. This low-mass progenitor is compatible with the small ionized nebular mass (1.3×10^{-2} – 1.6×10^{-1} $M_\odot$) obtained for RWT 152.

(6) The multiple, non-point-symmetric bubbles observed in the bipolar lobes could be attributed to interaction of a fast wind with an inhomogeneous distribution of material at both sides of the equatorial torus. Nevertheless, as RWT 152 is an already evolved PN, the original mechanism for the formation of the multiple bubbles could be masked by other phenomena that have occurred through the evolution.

ACKNOWLEDGMENTS

This paper has been partially supported by grant AYA 2011-24052 (AA, ES), AYA 2011-30228-C3-01 (LFM), ESP2014-55996-C2-2-R (AU), and AYA2014-57369-C3-3-P (LFM) of the Spanish MINECO (all them co-funded by FEDER funds). We also acknowledge support from grant INCITE09 312191PR (AU, LFM, AA) of Xunta de Galicia, partially funded by FEDER funds, from grant PRX15/00511 (AU) of the Spanish MECD, and from grant 12VI20 (AU, LFM, AA) of the University of Vigo. AA also acknowledges support from FONDECYT through postdoctoral grant 3160364. Authors are very grateful to the staff on the El Roque de los Muchachos Observatory and specially to Antonio Cabrera for helping us to plan and reduce the observations successfully. We also thank Irene Pintos for her detailed explanations about the tunable filters. We acknowledge support from the Faculty of the European Space Astronomy Centre (ESAC). This research has made use of the SIMBAD database, operated at the CDS, Strasbourg (France), Aladin, NASA's Astrophysics Data System Bibliographic Services, and the Spanish Virtual Observatory supported from the Spanish MINECO through grant AYA2011-24052.

REFERENCES

Aller A., Miranda L. F., Olguín L., Vázquez R., Guillén P. F., Oreiro R., Ulla A., Solano E., 2015a, MNRAS, 446, 317
Aller A. et al., 2013, A&A, 552, A25
Aller A., Montesinos B., Miranda L. F., Solano E., Ulla A., 2015b, MNRAS, 448, 2822
Bianchi L., Bohlin R., Catanzaro G., Ford H., Manchado A., 2001, AJ, 122, 1538
Bloecker T., 1995, A&A, 299, 755
Cardelli J. A., Clayton G. C., Mathis J. S., 1989, ApJ, 345, 245
Cepa J. et al., 2003, in Revista Mexicana de Astronomia y Astrofisica Conference Series, Vol. 16, Revista Mexicana de As-

tronomia y Astrofisica Conference Series, Rodriguez Espinoza J. M., Garzon Lopez F., Melo Martin V., eds., pp. 13–18
Cepa J. et al., 2005, in Revista Mexicana de Astronomia y Astrofisica, vol. 27, Vol. 24, Revista Mexicana de Astronomia y Astrofisica Conference Series, Hidalgo-Gámez A. M., González J. J., Rodríguez Espinosa J. M., Torres-Peimbert S., eds., pp. 1–6
Costa R. D. D., Chiappini C., Maciel W. J., de Freitas Pacheco J. A., 1996, A&A, Supplement, 116, 249
De Marco O., 2009, PASP, 121, 316
Dorman B., Rood R. T., O'Connell R. W., 1993, ApJ, 419, 596
Ebbets D. C., Savage B. D., 1982, ApJ, 262, 234
Frew D. J., Parker Q. A., 2010, PASA, 27, 129
Gesicki K., Zijlstra A. A., 2003, MNRAS, 338, 347
González J. J., Cepa J., González-Serrano J. I., Sánchez-Portal M., 2014, MNRAS, 443, 3289
Guillén P. F., Vázquez R., Miranda L. F., Zavala S., Contreras M. E., Ayala S., Ortiz-Ambriz A., 2013, MNRAS, 432, 2676
Gurzadian G. A., Egikian A. G., 1991, Astrophysics & Space Science, 181, 73
Heber U., 2009, A&A Annual Review, 47, 211
Heber U., Dreizler S., Werner K., 1993, Acta Astron., 43, 337
Henry R. B. C., Kwitter K. B., Balick B., 2004, AJ, 127, 2284
Hillwig T. C., Bond H. E., Afşar M., De Marco O., 2010, AJ, 140, 319
Howard J. W., Henry R. B. C., McCartney S., 1997, MNRAS, 284, 465
Hua C. T., Kwok S., 1999, A&A, Supplement, 138, 275
Kaler J. B., Jacoby G. H., 1991, ApJ, 372, 215
Karakas A. I., 2010, MNRAS, 403, 1413
Kingsburgh R. L., Barlow M. J., 1994, MNRAS, 271, 257
Kwitter K. B., Henry R. B. C., 2001, ApJ, 562, 804
Maciel W. J., Koppen J., 1994, A&A, 282, 436
Marigo P., 2001, A&A, 370, 194
Olguín L., Vázquez R., Contreras M. E., Jiménez M. Y., 2011, in Revista Mexicana de Astronomia y Astrofisica, vol. 27, Vol. 40, Revista Mexicana de Astronomia y Astrofisica Conference Series, pp. 193–193
Østensen R. H., 2006, Baltic Astronomy, 15, 85
Osterbrock D. E., Ferland G. J., 2006, Astrophysics of gaseous nebulae and active galactic nuclei
Otsuka M., Hyung S., Tajitsu A., 2015, ApJ Supplements, 217, 22
Peña M., Rechy-García J. S., García-Rojas J., 2013, RMxAA, 49, 87
Peimbert M., 1978, in IAU Symposium, Vol. 76, Planetary Nebulae, Terzian Y., ed., pp. 215–223
Peimbert M., 1990, Reports on Progress in Physics, 53, 1559
Peimbert M., Torres-Peimbert S., 1983, in IAU Symposium, Vol. 103, Planetary Nebulae, Flower D. R., ed., pp. 233–241
Pereira C. B., Miranda L. F., 2007, A&A, 467, 1249
Pritchet C., 1984, A&A, 139, 230
Quireza C., Rocha-Pinto H. J., Maciel W. J., 2007, A&A, 475, 217
Ramos-Larios G., Phillips J. P., 2009, MNRAS, 400, 575
Rauch T., 1999, A&A, Supplement, 135, 487
Ressler M. E., Cohen M., Wachter S., Hoard D. W., Mainzer A. K., Wright E. L., 2010, AJ, 140, 1882
Rijkhorst E.-J., Mellema G., Icke V., 2005, A&A, 444, 849
Sahai R., 2000, ApJ Letters, 537, L43
Sahai R., Trauger J. T., 1998, AJ, 116, 1357
Schlegel D. J., Finkbeiner D. P., Davis M., 1998, ApJ, 500, 525
Schoenberner D., 1983, ApJ, 272, 708
Seaton M. J., 1979, MNRAS, 187, 73P
Shaw R. A., Dufour R. J., 1995, PASP, 107, 896
Steffen W., Koning N., Esquivel A., García-Segura G., García-Díaz M. T., López J. A., Magnor M., 2013, MNRAS, 436, 470
Velázquez P. F., Raga A. C., Riera A., Steffen W., Esquivel A., Cantó J., Haro-Corzo S., 2012, MNRAS, 419, 3529
Weidmann W. A., Gamen R., 2011, A&A, 526, A6